

Mechanical property measurement of InP-based MEMS for optical communications

Marcel W. Pruessner^{a,b}, Todd T. King^c, Daniel P. Kelly^{a,b}, Rohit Grover^b,
Lynn C. Calhoun^b, Reza Ghodssi^{a,b,*}

^a MEMS Sensors and Actuators Laboratory (MSAL), Department of Electrical and Computer Engineering,
The Institute for Systems Research (ISR), A.V. Williams Building, University of Maryland, College Park, MD 20742, USA

^b Laboratory for Physical Sciences (LPS), 8050 Greenmead Drive, College Park, MD 20740, USA

^c NASA Goddard Space Flight Center (NASA-GSFC), Greenbelt, MD 20771, USA

Received 25 November 2002; accepted 31 March 2003

Abstract

We investigate mechanical properties of indium phosphide (InP) for optical micro-electro-mechanical systems (MEMS) applications. A material system and fabrication process for InP-based beam-type electrostatic actuators is presented. Strain gradient, intrinsic stress, Young's modulus, and hardness are evaluated by beam profile measurements, nanoindentation, beam bending, and electrostatic testing methods. We measured an average strain gradient of $\delta\varepsilon_0/\delta t = 4.37 \times 10^{-5} \mu\text{m}^{-1}$, with an average intrinsic stress of $\sigma_0 = -5.4$ MPa for [0 1 1] beams. The intrinsic stress results from arsenic contamination during molecular beam epitaxy and (MBE) can be minimized by careful MBE growth and through the use of stress compensating layers. Nanoindentation of (1 0 0) InP resulted in $E = 106.5$ GPa and $H = 6.2$ GPa, while beam bending of [0 1 1] doubly clamped beams resulted in $E = 80.4$ GPa and $\sigma_0 = -5.6$ MPa. We discuss the discrepancy in Young's modulus between the two measurements. In addition, we present a method for simultaneously measuring Young's modulus and residual stress using beam bending. Electrostatic actuation in excess of 20 V is demonstrated without breakdown. © 2003 Elsevier Science B.V. All rights reserved.

Keywords: Optical MEMS; InP; Nanoindentation; Bending test; MBE growth

1. Introduction

1.1. Wavelength-division multiplexed communications

In time-division multiplexing (TDM), each signal is transmitted for a time interval, after which the next signal is transmitted for the next time interval and so forth. Consequently, the capacity of a TDM communications channel is limited by the data rate available [1]. In wavelength-division multiplexing (WDM) many signals (wavelengths) are transmitted simultaneously over the same communications channel. This increases the capacity of the network significantly without deployment of more optical fibers, an expensive undertaking [1]. In WDM, the capacity of the network is determined by the number of distinct wavelengths that can be transmitted simultaneously. Typically, wavelengths are separated by 10–100 nm in WDM. Future dense-WDM (DWDM) systems may have wavelengths spaced less than 1 nm [2].

The advent of WDM and DWDM has created a need for various micro-optical components including tunable lasers, variable attenuators and equalizers, optical filters and demultiplexers, and optical cross-connect switches. Tunable lasers are significantly cheaper than multiple fixed-wavelength laser sources and are therefore preferred for WDM networks. Variable attenuators can equalize the spectrum and can help compensate for dispersion and other non-linear behavior of the optical channel. Optical filters are needed to separate the wavelengths transmitted over the communications channel, so that they may be directed to individual users. Finally, optical cross-connect switches are needed to direct traffic between various network nodes.

Recently, there has been considerable interest in using micro-electro-mechanical systems (MEMS) technology for optical switches in network applications [1,3,4]. The reasons are simple: the required displacements in optical switches and tunable optical filters are of the order of a few wavelengths (micrometers) and are thus well suited to low power MEMS actuators. Also, the potential for batch fabrication enables huge cost savings compared to

* Corresponding author. Tel.: +1-301-405-8158; fax: +1-301-314-9281.
E-mail address: ghodssi@eng.umd.edu (R. Ghodssi).

macro-scale switching networks and enables scaling up to a large number of elements on a single chip.

1.2. InP-based MEMS

Typically, MEMS devices are made from silicon, which has an indirect bandgap and is unsuitable for active optoelectronic devices. In contrast, InP is a direct bandgap semiconductor ($E_g = 1.34 \text{ eV}$ [5]), and can be used in active optoelectronic devices, such as lasers and semiconductor optical amplifiers. By incorporating such active devices in a MEMS platform, losses can be compensated on-chip.

Compound semiconductors of the $\text{In}_x\text{Ga}_{1-x}\text{As}_y\text{P}_{1-y}$ family can be grown lattice-matched to InP substrates with tailored bandgaps [5]. Existing fiber optic cables exhibit minimal losses at 1550 nm. Therefore, most modern optical communications systems operate around 1550 nm.

Monolithic integration of existing active optoelectronics with InP-based MEMS actuators will enable novel and versatile WDM optoelectronic devices. However, before InP-based optical MEMS can be realized, the mechanical properties of this material must be characterized to ascertain its applicability to micro-mechanical devices. Few groups have studied the mechanical properties of InP for MEMS applications and very few InP-based MEMS devices have been reported in the literature [6–9].

The motivation for this research is, therefore, the development of a platform and fabrication process for InP-based MEMS electrostatic actuators and assessment of the mechanical properties of InP for optical MEMS applications. We accomplish this by using InP microbeam electrostatic actuators. Future work will focus on monolithic integration of optoelectronic technology with InP-based MEMS, enabling novel optical components for high-speed WDM networks.

2. Sample preparation

MEMS mechanical property measurement is performed using InP cantilever and doubly clamped microbeams. We discuss the theory behind each measurement technique in Section 3. The layer structure in Fig. 1 consists of a doped (100) InP substrate ($n = 3 \times 10^{18} \text{ cm}^{-3}$), on which we grow a $0.4 \mu\text{m}$ thick InP buffer layer

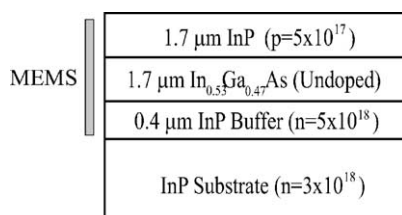


Fig. 1. InP-based MEMS layer structure.

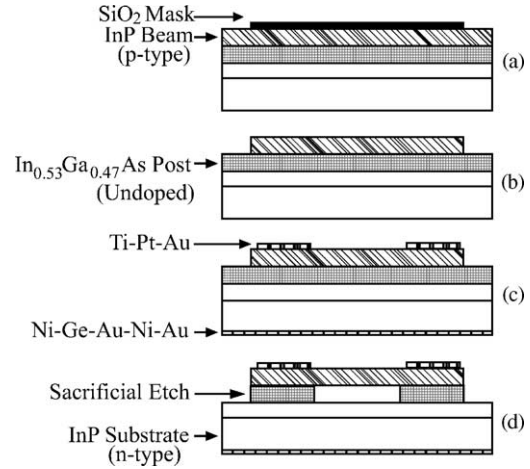


Fig. 2. InP beam-type electrostatic actuator process flow: (a) pattern SiO_2 mask; (b) pattern transfer into InP by methane–hydrogen–argon RIE; (c) remove SiO_2 mask and deposit p- and n-side metal contacts, and pattern p-side metal by lift-off, followed by an anneal at 400°C to alloy the n-side metal; (d) pattern photoresist mask to define the beam posts; etch sacrificial InGaAs layer with $\text{H}_2\text{SO}_4:\text{H}_2\text{O}_2:\text{H}_2\text{O}$ (1:1:8) followed by supercritical CO_2 drying to prevent stiction.

($n = 5 \times 10^{18} \text{ cm}^{-3}$), followed by an intrinsic $1.7 \mu\text{m}$ thick $\text{In}_{0.53}\text{Ga}_{0.47}\text{As}$ sacrificial layer and a $1.7 \mu\text{m}$ thick p-doped InP beam layer ($p = 5 \times 10^{17} \text{ cm}^{-3}$). The dimensions were chosen because they represent thickness similar to those used for optical waveguides. During operation, the beam post is a reverse-biased p–i–n junction, which acts as an insulator.

The cantilever and doubly clamped beams are 16 and $40 \mu\text{m}$ wide, with beam lengths ranging from 100 to $1000 \mu\text{m}$ in $50 \mu\text{m}$ increments, and 1100 – $1500 \mu\text{m}$ in $100 \mu\text{m}$ increments, oriented along the $[011]$ and $[0\bar{1}0]$ directions. The basic process flow is shown in Fig. 2. Using a 500 nm -thick SiO_2 mask, we etched the InP beam layer with methane–hydrogen–argon in a Plasmatherm 790 series reactive ion etching (RIE) system [10]. After patterning the beams, we deposited Ni–Ge–Au–Ni–Au on the backside of the n-type substrate by electron beam evaporation. Next, we deposited Ti–Pt–Au on the p-type InP beam layer and patterned it by lift-off. We alloyed the backside contact at 400°C in an N_2/H_2 atmosphere [11]. Then, we patterned a photoresist mask to define the beam posts and released the beams by etching the sacrificial layer ($1.7 \mu\text{m}$ InGaAs) in $\text{H}_2\text{O}_2:\text{H}_2\text{SO}_4:\text{H}_2\text{O}$ (1:1:8). A typical etch time was 19 min with a measured InGaAs etch rate of 3.33 and $1.5 \mu\text{m}/\text{min}$ for the major $[011]$ and minor $[0\bar{1}1]$ directions without agitation, respectively. Note that the beams are oriented along the major direction, so our etch rate is along the minor direction ($1.5 \mu\text{m}/\text{min}$). In order to ensure complete sacrificial etching, we placed the samples in the etchant and agitated the solution with a glass rod to provide for continuous flow of etchant underneath the beams. This step is especially necessary for proper release of the $40 \mu\text{m}$ wide beams. We avoided stiction by

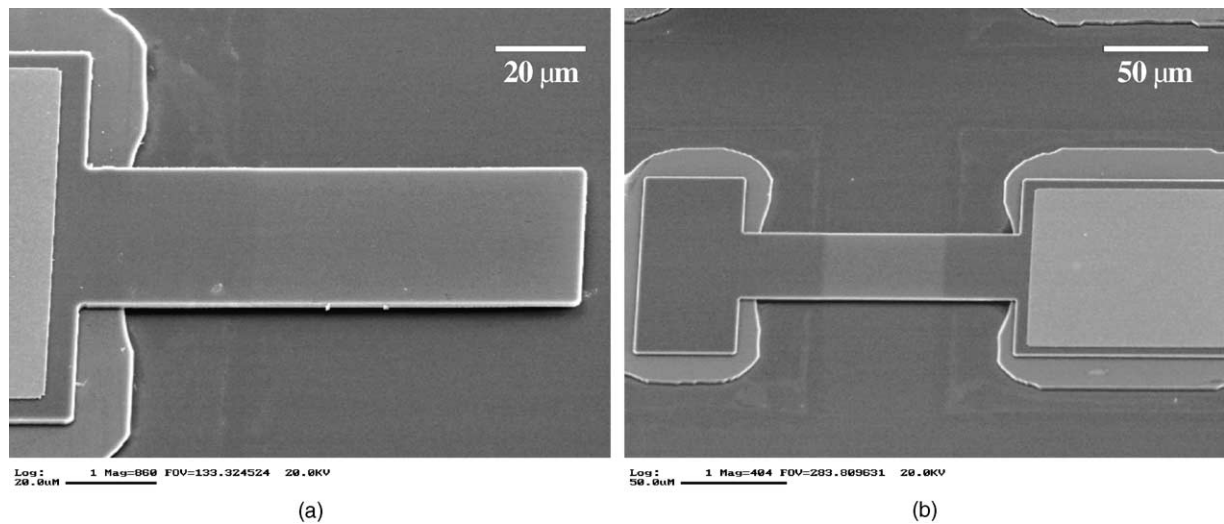


Fig. 3. (a) Cantilever beam (left); (b) doubly clamped beam (right). We etched the InP beam with methane–hydrogen–argon gas in a Plasmatherm 790 RIE system. The beam thickness is 1.7 μm and the beam–substrate gap is 1.7 μm.

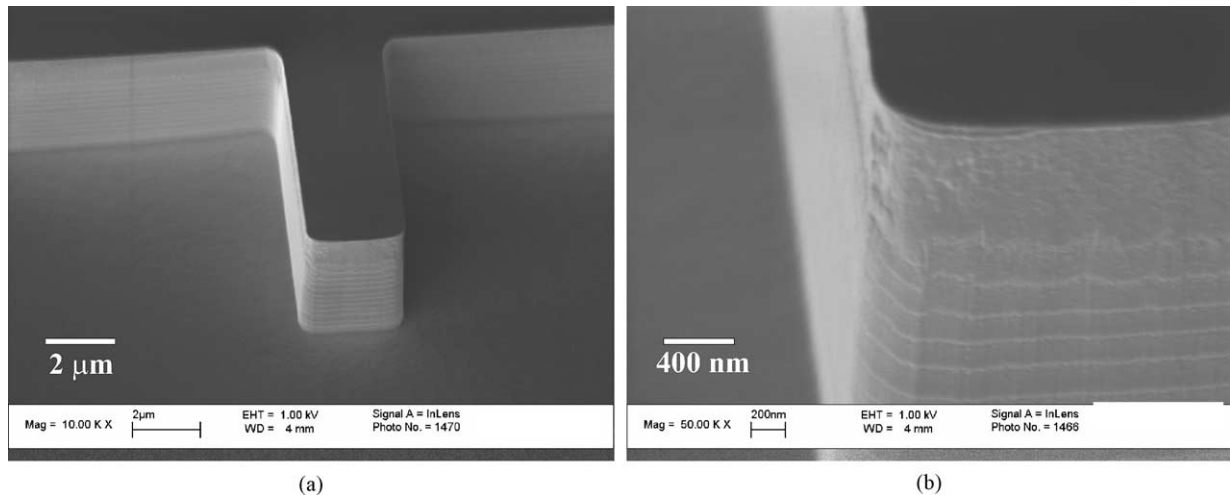


Fig. 4. (a) InP test etch using SiO₂ mask, with methane–hydrogen RIE, after SiO₂ mask removal and sample clean (left); (b) sidewall roughness is ~20 nm with verticality of 89° or better (right). The roughness at the top portion of the sidewall is due to a wet etching step in order to clean the device after a partial etch of 1 μm. The total etch depth is 3.6 μm.

utilizing supercritical CO₂ drying after the sacrificial release step.

Fabricated cantilever and doubly clamped beams are shown in Fig. 3. The argon used in our earlier methane–hydrogen–argon RIE process caused wear of the alumina carrier used in the Plasmatherm 790 RIE system. Over time, this exposed the underlying aluminum. Aluminum sputters easily and was deposited on the samples during etching, resulting in nanograss from micro-masking. Therefore, we modified the etch process to use only methane–hydrogen RIE. Using this modified process, we obtained extremely smooth (~20 nm sidewall roughness), 3.6 μm tall vertical sidewalls (89° or better), as shown in Fig. 4. The importance of thorough cleaning and conditioning of the RIE chamber was reinforced during development of the modified process, especially

since the clean room is a multi-user facility with many different materials being processed in the same etch chamber.

3. Theory

While some reports of InP-based MEMS can be found in the literature [6–9], very few efforts have concentrated on studying the mechanical properties of this material for MEMS applications in detail. In this work, we use cantilever curvature and beam buckling measurements [12–14] for extraction of the strain gradient and intrinsic compressive stress. We chose three methods for micro-mechanical property measurements: nanoindentation [15–17], beam bending [13,17,18], and electrostatic testing [19]. We

now review the principle and theory governing each technique.

3.1. Strain gradients and intrinsic compressive stress

Out-of-plane curvature of cantilevers and doubly clamped beams enables measurement of strain gradients along the thickness of the material as well as an average *compressive* stress along the beam length. The strain gradient can be measured by the self-deflection of cantilevers [12]:

$$\frac{\delta\varepsilon_0}{\delta t} = \frac{z}{L^2} = \frac{1}{R}, \quad (1)$$

where $\delta\varepsilon_0/\delta t$ is the strain gradient along the thickness of the beam, z the vertical deflection at the beam end (positive or negative), L the cantilever beam length, and R the radius of curvature of the beam. The stress gradient is then found by $\delta\sigma/\delta t = E(\delta\varepsilon/\delta t)$.

If doubly clamped beams are under sufficient compressive stress exceeding the *Euler Buckling limit* [13], then the beams buckle and assume a cosine shape. Note that beams with *tensile* stress will remain flat. The total compressive strain, ε_0 , of the buckled beam includes the Euler strain as well as the axial strain and can be derived as

$$\varepsilon_0 = \varepsilon_a + \frac{\sigma_{\text{Euler}}}{E} = -\frac{\pi^2}{L} \left(\frac{z^2}{4} + \frac{t^2}{3} \right), \quad (2)$$

where ε_a is the axial strain, $\varepsilon_{\text{Euler}} = \sigma_{\text{Euler}}/E$, L the doubly clamped beam length, z the maximum out-of-plane deflection (buckling) at the beam center, t the beam thickness, and E the Young's modulus. Eq. (2) can be rewritten to give the result for multi-layer materials [14]. By measuring the out-of-plane deflection z of doubly clamped beams of length L and thickness t , the total *compressive* strain can be extracted. The intrinsic stress can be calculated as $\sigma = \varepsilon E$.

3.2. Nanoindentation

In nanoindentation [15–17], a load is applied to a thin film or bulk substrate using a Berkovich tip, which con-

sists of a three-side diamond pyramid with a radius of a few micrometers [20]. Other types of indenter tips are also commonly used in nanoindentation. The load, typically a 100 μN to a few mN, is applied electrostatically and the resulting tip displacement is measured capacitively (Fig. 5(a)). The nanoindenter consists of a scanning probe microscope (Digital Instruments, Dimension 3000 SPM [21]) with an add-on nanoindentation system (Hysitron Inc., Triboscope Nanomechanical Test Instrument [20]; Fig. 5(b)).

A typical load–time diagram is shown in Fig. 6(a). During loading, both elastic and plastic deformation occur. During hold, the material is allowed to settle, and during unloading only the elastic deformation is recovered. For this reason, a hysteresis can be observed in the load–displacement diagram (Fig. 6(b)). The elastic deformation (unloading) enables measurement of Young's modulus, while the maximum indent depth and plastic deformation enable measurement of the material hardness.

The important parameters in a load–displacement measurement are the maximum applied load, P_{max} , the maximum indent depth, h_{max} , and the maximum residual depth after unloading, h_f . From the linear portion of the unload curve in Fig. 6(b), the elastic contact stiffness, S , can be obtained by [15,16]

$$S = \frac{dP}{dh}. \quad (3)$$

The hardness (H) and Young's modulus (E_f) can then be extracted by [15,16]

$$E_r = \frac{\sqrt{\pi}}{2\beta} \frac{S}{\sqrt{A}}, \quad (4)$$

$$H = \frac{P}{A}, \quad (5)$$

and

$$\frac{1}{E_r} = \frac{1 - \nu_f^2}{E_f} - \frac{1 - \nu_i^2}{E_i}, \quad (6)$$

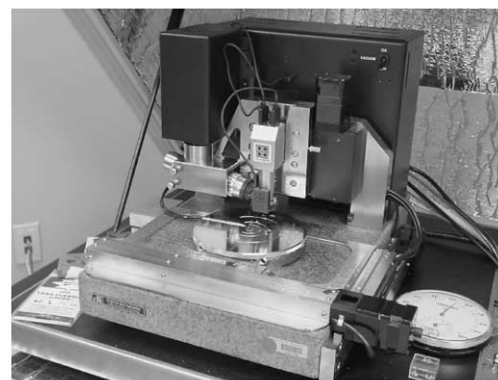
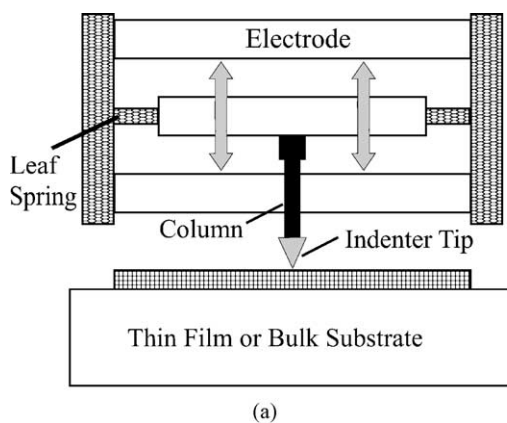


Fig. 5. (a) Nanoindenter schematic with electrostatic actuation and capacitive displacement sensing (left); (b) digital instruments SPM with Hysitron nanoindenter used in the experiments (right).

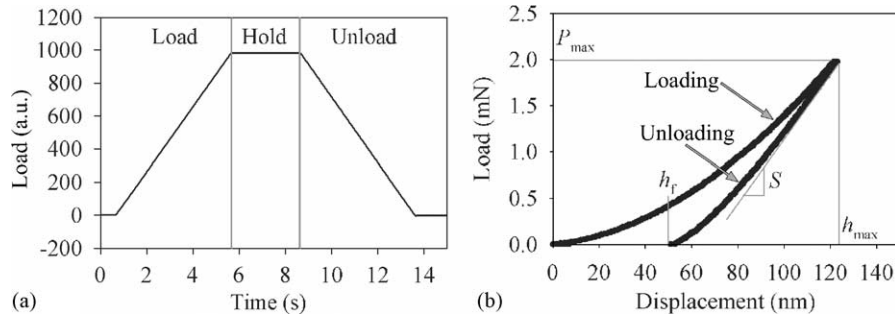


Fig. 6. (a) Trapezoidal load–time diagram for a single indent (left); (b) measured load–displacement for a fused-quartz calibration sample. The hysteresis results from plastic deformation during loading (right).

where A is the projected contact area under load, β a constant that depends on the geometry of the indenter tip, ν the Poisson's ratio, ' r ' denotes the reduced modulus and describes the contribution of both the nanoindenter tip and the material to be tested, ' f ' denotes the modulus of the material of interest (i.e. thin film or bulk substrate), and ' i ' denotes the indenter tip. Using this notation, the Young's modulus of the thin film or bulk substrate is denoted as E_f . Typically, the indenter tip is much harder than the measured material (for a diamond indenter tip, $E_i = 1140$ GPa, $\nu_i = 0.07$ [15]).

3.3. Beam bending

In beam bending we use the nanoindenter to apply a point load to microbeams (Fig. 7). Nanoindentation enables the measurement of both Young's modulus (E) and hardness (H), while beam bending (cantilever or doubly clamped) measures E . Bending of doubly clamped beams also enables the measurement of intrinsic stress (σ_0). An advantage of beam bending is that it enables the measurement of E along the direction of the beam. Thus, one can measure Young's modulus along arbitrary crystal orientations. Although beam bending can also be performed on cantilevers, we will treat only doubly clamped beams here since the fabricated cantilever beams were too compliant to be tested.

In beam bending we use a conical diamond tip with $5\ \mu\text{m}$ tip radius and 60° cone angle. This ensures that we bend the beam and do not indent it. For beam bending, the applied loads are typically $10\text{--}100\ \mu\text{N}$, with the load determined by the spring stiffness of the beam. Note that the stiffness of the doubly clamped beam is much greater than that of the nanoindenter, so that we do not need to subtract the contribution of the nanoindenter from the beam bending behavior. For very compliant beams, such as cantilevers, this repre-

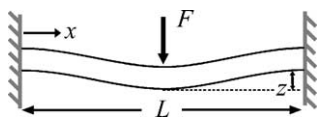


Fig. 7. Bending of a center-loaded doubly clamped beam: F is the applied load, L the beam length, x the distance from one end of the beam to the point of applied load, and z the vertical displacement.

sents a significant error that needs to be accounted for, but for doubly clamped beams the error is insignificant.

A typical doubly clamped beam bending load–displacement curve is shown in Fig. 8. For small loads, the dependence is linear, while at larger loads the displacement becomes a non-linear function of the applied force. The spring stiffness, S , for a doubly clamped beam consists of three separate terms due to bending, stress, and stretching components. The bending and stress components dominate at small loads, and at large loads the stretching term dominates. The sum of the individual terms gives the complete beam bending behavior for doubly clamped beams with center point load [13]:

$$F = k_{\text{bending}}z + k_{\text{stress}}z + k_{\text{stretching}}z^3$$

$$= \frac{Ew\pi^4}{6} \left(\frac{t}{L}\right)^3 z + \frac{w\sigma_0\pi^2}{2} \left(\frac{t}{L}\right)z + \frac{Ew\pi^4}{8} \left(\frac{t}{L^3}\right)z^3, \quad (7)$$

where E is the Young's modulus, w the beam width, t the beam thickness, L the beam length, σ_0 the intrinsic stress, F the load applied at the beam center, and z the resulting beam deflection.

Note that (7) is an approximate equation. It gives the functional form of the beam bending equation, including all contributions of bending, intrinsic stress, and beam stretching. A more accurate solution should include simulations [13] to determine the precise solution. Nonetheless, a comparison

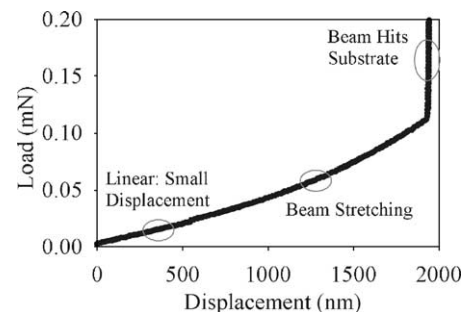


Fig. 8. Doubly clamped beam bending load–displacement measurement. At small displacements the bending behavior is linear while at larger displacements the beam stretches and introduces a non-linearity.

of the approximate k_{bending} in (7) and the exact solution for k_{bending} [18] results in an error of less than 1.5%, indicating that the approximate solution is accurate to within a few percent.

Also, the reader should be aware that the measured modulus is actually the plate modulus, E_{Plate} , since the beams are designed such that $w > 5t$ [19]:

$$E_{\text{Plate}} = \frac{E}{1 - \nu^2}, \quad (8)$$

where ν is the Poisson's ratio. However, for the [0 1 1] beam direction, ν is 0.020 [23] so $E_{\text{Plate}} \cong E$ and we do not need to distinguish between the two.

If the residual stress, σ_0 , of the beam is known, then a beam bending experiment in the small displacement (linear) region enables the measurement of Young's modulus. If σ_0 is not known, then data from beam bending experiments on an array of doubly clamped beams with different lengths enables measurement of both E and σ_0 simultaneously (Section 4.3).

3.4. Electrostatic testing

In M-test [19], an electrostatic pressure load is used to deflect beams in a manner similar to beam bending (Fig. 7). Electrostatically actuated beams exhibit an instability that causes them to be "pulled-in" once the applied voltage exceeds the pull-in voltage, V_{PI} (Fig. 9). By measuring V_{PI} , Young's modulus and intrinsic stress of thin films can be measured. Either cantilever or doubly clamped beams can be used.

Note that cantilevers, by nature, are not affected by intrinsic stress, since the sacrificial release of these beams allows for the stress—either compressive or tensile—to be relieved. Cantilevers are affected significantly by strain stress gradients, however assuming negligible stress gradients, only Young's modulus can be extracted from cantilevers. Doubly clamped beams also enable intrinsic stress extraction since their bending behavior is influenced by intrinsic stress [19].

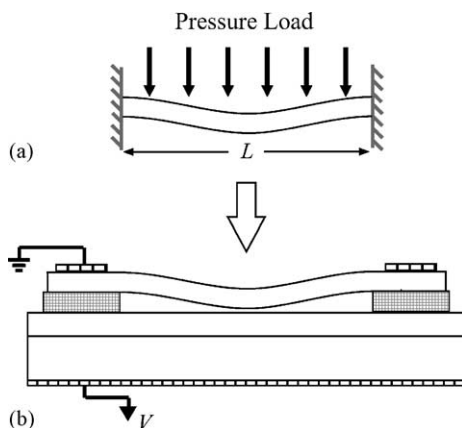


Fig. 9. Electrostatically actuated beam: (a) beam bending with uniform pressure load (top) and (b) electrostatic pressure load (bottom).

A typical experiment requires measuring V_{PI} for a set of beams with different lengths, preferably spanning the range from bending (short) to stress dominated (long). Both E and σ_0 are then extracted by curve-fitting [19].

The analytical form for the pull-in voltage of a beam is given by [19]

$$V_{\text{PI}} = \sqrt{\frac{8K_{\text{eff}}g_0^3}{27\varepsilon_0[1 + 0.42(g_0/w)]}}, \quad (9)$$

where K_{eff} is the effective spring constant of the cantilever or doubly clamped beam, g_0 the original beam–substrate gap, ε_0 the free-space permittivity, and w the beam width. A more detailed solution is presented in Ref. [19].

M-test is convenient because the measurement setup is contained on-chip, and unlike nanoindentation and bending tests, no external measurement setup is required other than a power supply and an optical microscope to observe pull-in. A significant drawback of this method, however, is the requirement that the beams be flat since the electrostatic force is a quadratic function of the beam-to-substrate gap. Also, the material to be tested must be conducting; insulators cannot be characterized.

4. Experimental results

4.1. Strain gradients and intrinsic compressive stress

Out-of-plane curvature of cantilevers is shown in Fig. 10(a), and buckling of doubly clamped beams is shown in Fig. 10(b). We measured the cantilever beam curvature and doubly clamped beam buckling using a confocal microscope (Nikon MM-40 measuring microscope and Lasertec 1LM21 laser microscope) and used curve-fitting to extract the strain gradient (Fig. 10(c)) and compressive strain (Fig. 10(d)). The vertical resolution of the confocal microscope is, ideally, the maximum height profile measured divided by 256, the number of levels that the microscope measures. However, due to noise the maximum vertical resolution is in the 100 nm range and depends on the objective lens used.

The strain gradient was $4.37 \times 10^{-5} \mu\text{m}^{-1}$ (four measurements on one chip) resulting in a stress gradient of 4.06 MPa/ μm . The intrinsic compressive strain was 5.85×10^{-5} (nine measurements on two chips), resulting in an intrinsic compressive stress of -5.4 MPa. For stress extraction we assumed a Young's modulus of 93 GPa for the [0 1 1] direction [23].

Although the layer structure was designed to be lattice-matched—so ideally the material should be stress-free—the measured strain causes significant beam curvature and buckling. We believe that residual arsenic in the molecular beam epitaxy (MBE) chamber as well as arsenic in the underlying InGaAs layer was inadvertently incorporated into the InP beam layers during growth. This contamination

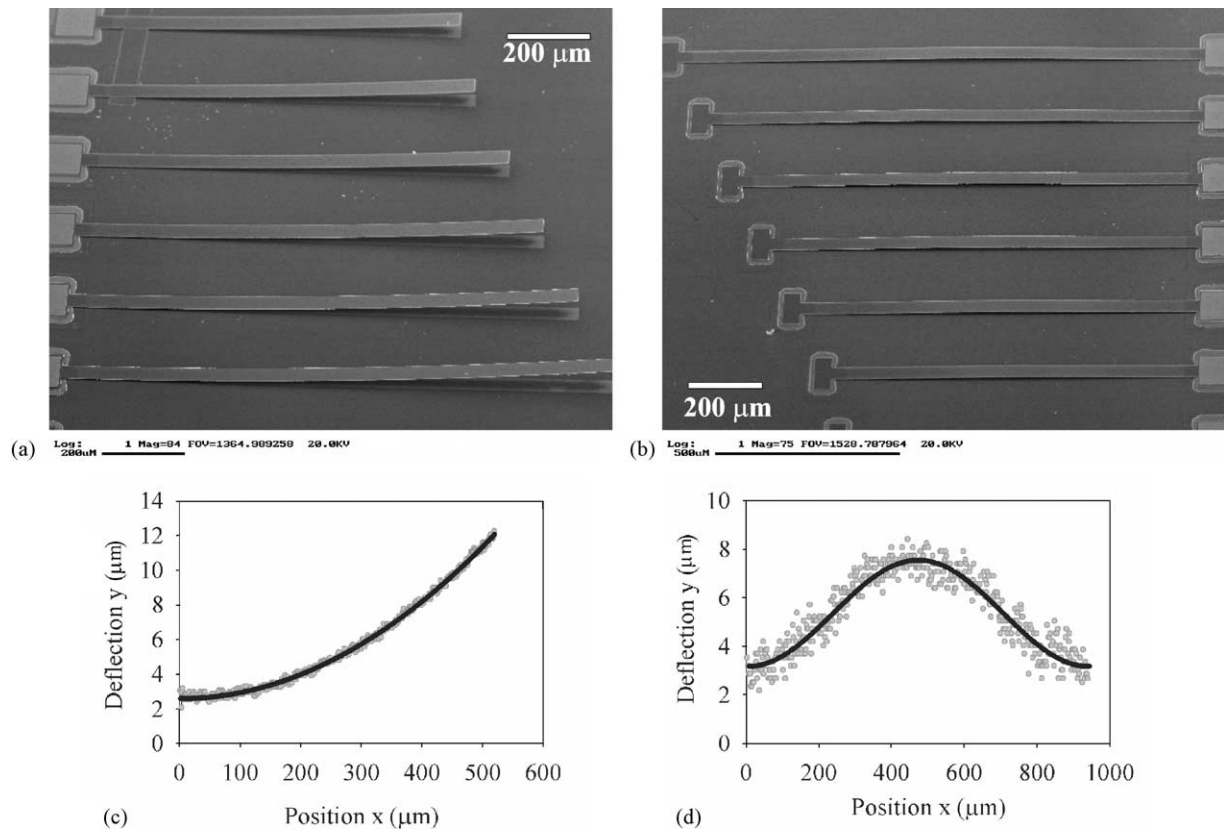


Fig. 10. (a) Cantilever deflection due to strain gradient (top left); (b) doubly clamped beam buckling due to compressive stress (top right); (c) measured deflection and curve fit for 550 μm long cantilever beam (bottom left); (d) measured buckling and curve fit for 950 μm long doubly clamped beam (bottom right) and x denotes the location along the beam length. All beams are along the [011] direction.

led to compressive stress as well as the strain gradient since the amount of arsenic diminishes as thicker InP is grown. The presence of residual arsenic is confirmed by X-ray diffraction measurements, which indicate an average arsenic mole fraction of 0.0026 so that the ‘InP beam layer’ consists of $\text{InAs}_{0.0026}\text{P}$. The resulting compressive strain is calculated to be 8.4×10^{-5} , which is in general agreement with the compressive strain measured by beam buckling. The strain gradient and compressive stress measured by beam deflection and X-ray diffraction are smaller than those reported in Ref. [9] for similar InP growths, although of the same order of magnitude.

4.2. Nanoindentation

We performed nanoindentation experiments on bulk InP substrates and on the various epitaxial layers of the MBE grown wafer (Fig. 11). Prior to the nanoindentation experiments, a fused-quartz sample was used to calibrate the nanoindenter. The calibration method [22] measures the ‘‘contact area function’’, from which A is derived, as well as the nanoindenter compliance. The method works well as long as non-idealities such as ‘‘pile-up’’ or ‘‘sink-in’’ [15] do not occur. We did not observe either of these non-ideal effects in our nanoindentation experiments, in-

dicating that the calibration technique in Ref. [22] is applicable.

We measured Young’s modulus and hardness using the nanoindenter setup in Fig. 5, and the included data acquisition software [20] allowed us to make automated measurements. The results are summarized in Table 1. An average Young’s modulus of 106.5 GPa and a hardness of 5.8 GPa (from ~ 100 measurements on four chips) was measured for all the InP layers. The bulk and buffer InP layers were n-type and had a slightly smaller Young’s modulus, E , than the p-type beam layer. In contrast, the hardness, H , of the two n-type layers was slightly larger than that of the p-type beam layer. This may be the result of ‘‘lattice hardening’’

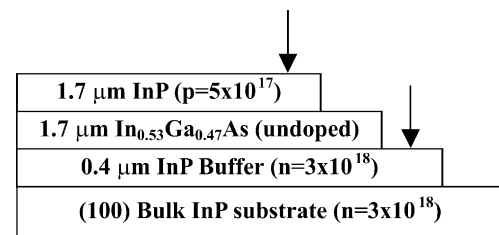


Fig. 11. Epitaxial layers used for nanoindentation. Bulk InP measurements were performed on blank (100) InP samples with $n = 3 \times 10^{18} \text{ cm}^{-3}$ (not shown).

Table 1
Nanoindentation results

Layer	E (GPa)	H (GPa)
Bulk InP (n-type)	104.8 ± 3.1 ($\pm 3.0\%$)	6.53 ± 0.21 ($\pm 3.3\%$)
InP buffer (n-type; $0.4 \mu\text{m}$)	105.8 ± 6.2 ($\pm 5.9\%$)	6.98 ± 0.32 ($\pm 4.6\%$)
InP epilayer (p-type; $1.7 \mu\text{m}$)	108.9 ± 4.0 ($\pm 4.3\%$)	6.08 ± 0.69 ($\pm 11.4\%$)

due to the different bond strengths and mechanical action of the dopant impurities [24].

4.3. Beam bending

We performed bending tests on beams with length less than $250 \mu\text{m}$ for displacements less than $0.5 \mu\text{m}$. The small displacement resulted in a linear load–displacement curve for all measured beams (Fig. 8). At displacements larger than $0.8 \mu\text{m}$, the beam stretching term in Eq. (7) becomes significant and the load–displacement curve becomes non-linear. Assuming negligible intrinsic stress, that is, considering only k_{bending} , we extracted an average Young’s modulus of 65.9 GPa with a standard deviation of 10.3 GPa (15.7%) from the load–displacement measurements. However, only short beams are truly ‘bending-dominated’. Longer beams are influenced significantly by intrinsic stress resulting in a reduced measured E for increasing doubly clamped beam length, L , as shown in Fig. 12(a). Fig. 12(b) shows the measured Young’s modulus, including the effects of compressive stress ($\sigma_0 = -5.4 \text{ MPa}$ obtained by beam buckling mea-

surements in Section 4.1). The average Young’s modulus is 80.4 GPa (18 measurements on two chips), with a standard deviation of 7.9 GPa (9.8%). The results in Fig. 12(a) and (b) illustrate the effects of intrinsic stress on the mechanical behavior of MEMS devices and emphasize the need for accurate stress characterization of MEMS materials.

An alternate method enables simultaneous measurement of Young’s modulus and residual stress, similar to electrostatic bending tests [19]. The beam stiffness is dominated by the Young’s modulus in short beams, and by intrinsic stress in long beams. Hence, by plotting the measured stiffness of an array of doubly clamped beams of varying lengths and performing a curve fit, two parameters k_{bending} and k_{stress} can be extracted. k_{bending} dominates for short beams, and k_{stress} dominates for longer beams (Fig. 13). From k_{bending} and k_{stress} , we extract E and σ_0 , respectively. Using this method, we measured a Young’s modulus of 82.0 GPa , and intrinsic stress of -5.6 MPa , in good agreement with the previous results.

This combined E and σ_0 extraction method has several advantages over electrostatic testing methods. Beam flatness is not a critical issue. That is, beams with intrinsic compressive stress can also be measured. Further, the materials to be tested do not have to be conducting—any thin film, whether conducting or insulating, can be measured. A potential drawback with this method, however, is the need for a nanoindentation setup. In contrast, electrostatic testing can be performed with minimal equipment.

4.4. Electrostatic testing

Electrostatic testing requires measurements at suitably high operating voltages. We evaluated the p–i–n junction beam posts (Fig. 2) with respect to leakage current and

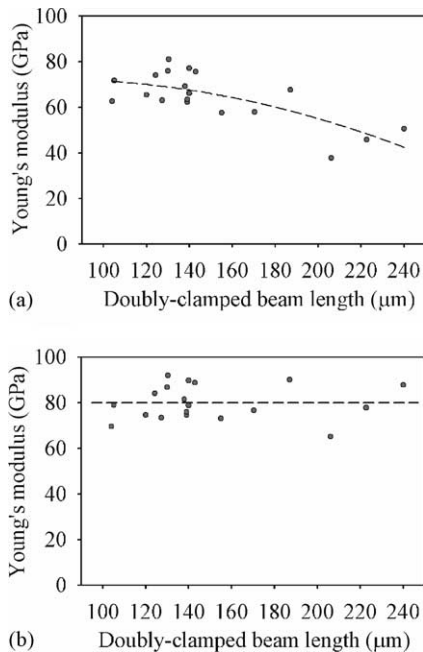


Fig. 12. (a) Extracted [011] Young’s modulus neglecting intrinsic compressive stress (top). The longer beams appear to be more compliant due stress. The average is 65.9 GPa with a standard deviation of 10.3 GPa (15.7%). (b) Extracted Young’s modulus assuming a compressive stress of $\sigma_0 = -5.4 \text{ MPa}$, obtained from beam buckling measurements (bottom). The average is 80.4 GPa with a standard deviation of 7.9 GPa (9.8%).

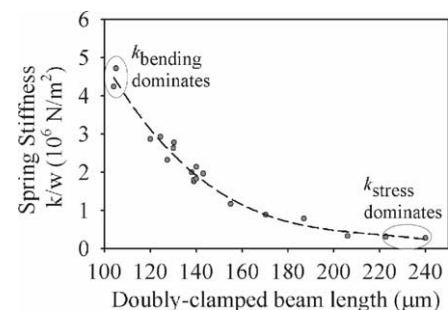


Fig. 13. Normalized beam spring stiffness k/w for [011] beams (k is the beam stiffness, w the beam width). k_{bending} and k_{stress} enable Young’s modulus (E) and intrinsic stress (σ_0) to be extracted, respectively.

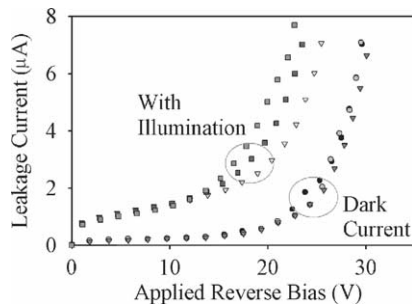


Fig. 14. Leakage current measurements on $110\ \mu\text{m} \times 110\ \mu\text{m}$ area, $1.7\ \mu\text{m}$ tall beam posts.

breakdown voltage. The breakdown voltage is in excess of 20 V (Fig. 14), so the present design is suitable for low-voltage InP electrostatic actuators required for optical MEMS. The 100 nA leakage current is significant. However, in the future we can use a semi-insulating (SI) substrate if we have lateral (in-plane) actuators, as envisioned for optical MEMS switches, rather than vertical (out-of-plane) actuators, as used in this study. In this manner we can minimize the leakage current through the InGaAs layer and can also increase the allowable operating voltage since we no longer need to be concerned with breakdown of our p–i–n junction.

Fig. 15 shows the Young's modulus extracted from an array of cantilevers with lengths 100–250 μm . The measurements are not consistent. At first glance, the cause would appear to be material non-uniformity. However, the inconsistency results from out-of-plane curvature of the cantilevers with increasing length due to strain gradients. This causes an increase in the applied electrostatic force needed for longer beams and skews the Young's modulus measurements. A similar problem occurred for the doubly clamped beams, which buckled due to compressive stress. Therefore, we were unable to measure mechanical properties with electrostatic testing. This did not impact the demonstration of InP-based MEMS actuation, however.

Electrostatic actuation is shown for a single doubly clamped beam viewed through a Nomarsky filter in Fig. 16. With increasing voltage, the fringes move towards the beam

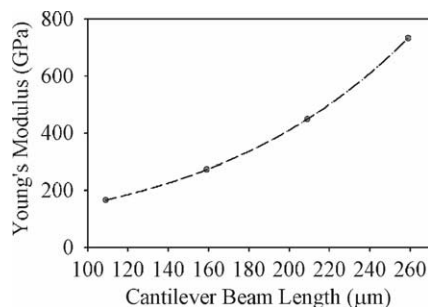


Fig. 15. Young's modulus extracted by electrostatic testing of an array of $[0\ 1\ 1]$ cantilevers. The increase in measured Young's modulus results from out-of-plane curvature of the cantilevers with increasing beam length.

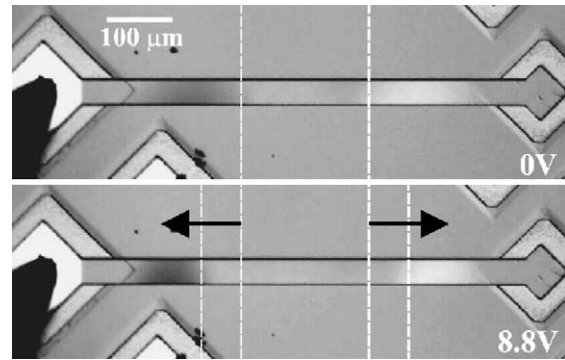


Fig. 16. Pull-in measurements on a $[0\ \bar{1}\ 0]$ doubly clamped beam viewed through a Nomarsky filter. Even with no applied voltage the doubly clamped beam buckles due to compressive stress, as seen by the presence of fringes (top). As the applied voltage is increased, the fringes move towards the beam ends, indicating that the beam bends down towards the substrate (bottom).

ends, indicating increased bending. The fringes are present even at zero applied voltage, indicating that the beam is not flat but buckles due to compressive stress.

The critical length at which buckling of doubly clamped beams occurs can be calculated from the *Euler Buckling stress*:

$$L_{\text{Critical}} = \sqrt{\frac{\pi^2}{3} \frac{Et^2}{\sigma_{\text{Euler}}}}, \quad (10)$$

assuming $E = 80\ \text{GPa}$ and $t = 1.7\ \mu\text{m}$, as measured for beams along the $[0\ 1\ 1]$ direction. This gives a critical length, $L_{\text{Critical}} = 650\ \mu\text{m}$. For the doubly clamped beam along the $[0\ \bar{1}\ 0]$ direction (Fig. 16), the Young's modulus is significantly smaller. Assuming $E = 61\ \text{GPa}$ (taken from Ref. [23], since we did not measure E for the minor direction), the critical buckling length is $L_{\text{Critical}} = 327\ \mu\text{m}$.

M-test requires measurements spanning the range from short and bending-dominated through long and stress-dominated. However, the critical length, L_{Critical} , prevents us from measuring the stress-dominated doubly clamped beams using electrostatic actuation.

4.5. Discussion

The mechanical properties of the epitaxially grown InP are summarized in Table 2. Note the orientation of the beams. Young's modulus is orientation dependent for InP and can vary significantly for other orientations [23]. Included in Table 2 are selected mechanical properties for gallium arsenide (GaAs) [23,27] and polysilicon [12,28–30] as a point of reference.

InP compares favorably with GaAs in terms of Young's modulus and hardness. Although not as robust as polysilicon, it can be used as a MEMS material. Electrostatic testing shows that InP is indeed suitable for electrostatic actuators used in MEMS. Further, optical devices typically require

Table 2
Summary of InP mechanical properties compared with GaAs [23,27] and polysilicon [12,28–30]

Property	(1 0 0) InP	Method	(1 0 0) GaAs	Polysilicon
Young's modulus (GPa)	106.5	Nanoindentation		156
	80.4 [0 1 1]	Beam bending	99.1 [0 1 1]	
Strain gradient (μm^{-1})	4.37×10^{-5}	Cantilever curvature	NA	$(1-4) \times 10^{-4}$
Intrinsic stress (MPa)	-5.4 [0 1 1]	Beam buckling	NA	-374.4 to +160
	-5.6 [0 1 1]	Beam bending		
Hardness (GPa)	6.2	Nanoindentation	6	11.0–11.4

displacements of the order of a few wavelengths (microns), so that low-voltage InP actuators are a good match.

A significant advantage of InP over GaAs concerns the wavelength at which lasers made from these materials can operate. Optical fibers have low losses at 1300 nm (~ 0.5 dB/km) and absolute minimum losses at 1550 nm (~ 0.2 dB/km) [25]. Although GaAs-based materials also enable active optoelectronic devices at 1300 nm, they do not exhibit gain around 1550 nm. InP-based lasers and semiconductor optical amplifiers can operate at 1550 nm. For this reason, it is desirable to work with InP.

InP MEMS and the mechanical property measurement approach taken in this research have some limitations. We highlighted the importance of good MBE growth coupled with effective device design in Section 4.1. Arsenic contamination results in stress gradients and compressive stress. This causes significant out-of-plane curvature of cantilevers and buckling of doubly clamped beams. Had these been optical devices, the result would have been a complete loss of functionality. In order to address the beam flatness issue, future devices will incorporate a trace amount of gallium to compensate for any arsenic contamination. The resulting layer structure, $\text{InGa}_{0.0xx}\text{As}_{0.0yy}\text{P}$, will enable a slight tensile strain to be introduced, resulting in flat doubly clamped devices. Preliminary growths have resulted in a tensile strain of 5.85×10^{-4} . Future growths will attempt to lower this strain to the 10^{-5} range. Note that the tensile strain should be kept small so as not to affect the mechanical properties of the material, as well as to minimize material dislocations. Thus, high quality optical thin films can be grown on top of the $\text{InGa}_{0.0xx}\text{As}_{0.0yy}\text{P}$ MEMS structure.

Another way to overcome material growth limitations is to work within the Euler Buckling Limit for doubly clamped beams:

$$\sigma_{\text{Euler}} = -\frac{\pi^2 Et^2}{3L^2}, \quad (11)$$

From (11) it is clear that we can compensate for any intrinsic compressive stress by careful device design (i.e. choosing L and t so that the magnitude of σ_{Euler} is greater than the magnitude of intrinsic compressive stress, σ_0 , of the material). A good optical MEMS design will also include doubly clamped devices instead of cantilevers. Cantilevers require extremely uniform material, while doubly clamped devices are relatively immune to strain (stress) gradients.

Table 2 shows a large variation in Young's modulus obtained by nanoindentation and beam bending measurements. This may be due to the directionality of nanoindentation measurements. Nanoindentation is extremely accurate for isotropic materials, but gives an average value for anisotropic materials such as InP. For example, the Young's modulus of single-crystal CuZn varies by less than 25% for different indentation orientations, despite its large anisotropy factor of 8 [26]. Consequently, the mechanical properties along individual crystal planes cannot be measured accurately.

Contrary to nanoindentation, which measures an average E , beam bending experiments measure Young's modulus along the length of the beam. InP is a crystal with anisotropic mechanical properties [23], and the elastic properties of the crystal differ significantly with orientation. Hence, the results obtained by nanoindentation and beam bending are not directly comparable.

Despite some limitations in these measurements—electrostatic testing could not be performed at all due to excessive beam curvature—this research has illustrated some fundamental issues for the development of InP-based MEMS. Material growth resulting in low stress epitaxial films is essential for MEMS. To achieve a desired bandgap for optoelectronic devices, however, we often need to work with strained materials. If this is the case, stress engineering and careful device design can be exploited to overcome any intrinsic stress within the MEMS structure. The combination of growth methods coupled with effective mechanical design will enable InP-based MEMS for optical communications.

5. Conclusions

We have presented a layer structure and process for fabricating simple InP-based beam-type electrostatic actuators. Our etch process enables low sidewall roughness (< 20 nm) with high verticality (89° or better), which is suitable for optical devices. The average strain gradient measured from cantilever curvature is $4.37 \times 10^{-5} \mu\text{m}^{-1}$ and the average intrinsic compressive stress from beam buckling measurements is -5.4 MPa. The compressive stress and the stress gradient are due to arsenic contamination of the InP epitaxial films during MBE growth. Careful MBE growth to reduce the arsenic contamination or stress engineering

methods will alleviate this problem. Nanoindentation gives a Young's modulus of 104.8–108.9 GPa and a hardness of 6.08–6.98 GPa. The variation in material properties is probably due to the effects of doping of the individual layers. We presented a method for simultaneously extracting Young's modulus and intrinsic stress from an array of doubly clamped beams. The method utilizes doubly clamped microbeam bending, and is suitable for both conducting and insulating films. This method gives a Young's modulus of 82.0 GPa, and intrinsic compressive stress of -5.6 MPa. Although we were not able to perform electrostatic measurements successfully due to excessive out-of-plane curvature of both cantilevers and doubly clamped beams, our simple beam-type structures successfully demonstrate InP-based MEMS actuation with breakdown voltages in excess of 20 V.

The micromechanical property measurement methods presented here are applicable to many materials, including metals, insulators, and semiconductors. Furthermore, this work has laid the foundation for InP-based optical MEMS. Future work will focus on the monolithic integration of InP-based MEMS with passive and active optoelectronic devices for WDM communications networks.

Acknowledgements

The authors thank Mr. L.C. Olver and the clean room staff at the Laboratory for Physical Sciences (LPS) for assistance with fabrication, and Mr. S.C. Horst and Capt. D. Hinkel for access to diagnostic and processing equipment at LPS. Prof. D. DeVoe, Mr. W.-J. Cheng, and Mr. F. Rosenberger are acknowledged for access to and assistance with the supercritical CO₂ dryer.

This research was supported by a National Science Foundation (NSF) CAREER award (Ghodssi) and by the LPS.

References

- [1] J.A. Walker, The future of MEMS in telecommunications networks, *J. Micromech. Microeng.* 10 (2000) R1–R7.
- [2] C.A. Brackett, Dense wavelength division multiplexing networks: principles and applications, *IEEE J. Sel. Areas Commun.* 8 (1990) 948–964.
- [3] A. Neukermans, R. Ramaswami, MEMS technology for optical networking applications, *IEEE Commun. Mag.* 39 (1) (2001) 62–69.
- [4] H. Fujita, H. Toshiyoshi, Optical MEMS, *IEICE Trans. Elec. E* 83 (2000) 1427–1430.
- [5] V. Swaminathan, A.T. Macrander, *Materials Aspects of GaAs and InP Based Structures*, Prentice-Hall, Englewood Cliffs, NJ, 1991.
- [6] P. Mounaix, P. Delobelle, X. Melique, L. Bornier, D. Lippens, Micromachining and mechanical properties of GaInAs/InP microcantilevers, *Mater. Sci. Eng. B* 51 (1998) 258–262.
- [7] S. Greek, K. Hjort, J.-A. Schweitz, C. Seassal, J.-L. Leclerq, M. Gendry, M.-P. Besland, P. Viktorovitch, C. Figuet, V. Souliere, Y. Monteil, The strength of indium phosphide based microstructures, *SPIE* 3008 (1997) 251–257.
- [8] P. Bondavalli, R. LeDantec, T. Benyattou, Influence of the involuntary underetching on the mechanical properties of tunable fabry-perot filters for optical communications, *J. MEMS* 10 (2001) 298–301.
- [9] M. Strasser, J. Daleiden, N. Chitica, D. Keiper, B. Stalnacke, S. Greek, K. Hjort, III–V semiconductor material for tunable fabry-perot filters for coarse and dense WDM systems, *Sens. Actuators A* 85 (2000) 249–254.
- [10] R. Grover, J.V. Hryniewicz, O.S. King, V. Van, Process development of methane–hydrogen–argon deep dry etching of InP for vertical facet-quality sidewalls, *J. Vac. Sci. Technol. B* 19 (2001) 1694–1698.
- [11] M.W. Pruessner, R. Grover, L. Calhoun, R. Ghodssi, Development of InP-based test structures for optical MEMS applications, in: *Proceedings of the International Symposium on Semiconductor Device Research*, Washington, DC, 2001, pp. 178–181.
- [12] J. Singh, S. Chandra, A. Chand, Strain studies in LPCVD polysilicon for surface micromachined devices, *Sens. Actuators A* 77 (1999) 133–138.
- [13] S.D. Senturia, *Microsystem Design*, Kluwer Academic Publishers, Boston, 2000.
- [14] S.A. Smee, M. Gaitan, D.B. Novotny, Y. Yoshi, D.L. Blackburn, IC test structures for multilayer interconnect stress determination, *IED Lett.* 21 (2000) 12–14.
- [15] J.L. Hay, G.M. Pharr (Eds.) *Instrumented indentation testing*, in: *ASM Handbook*, vol. 8, 10th ed., ASM, Materials Park, OH, 1990, pp. 232–243.
- [16] G.M. Pharr, W.C. Oliver, Measurement of thin film mechanical properties using nanoindentation, *MRS Bull.* 17 (1992) 28–33.
- [17] J.-A. Schweitz, Mechanical characterization of thin films by micromechanical techniques, *MRS Bull.* 17 (1992) 34–45.
- [18] S. Krenk, *Mechanics and Analysis of Beams, Columns, and Cables*, Springer, Berlin, 2001.
- [19] P.M. Osterberg, S.D. Senturia, M-TEST: a test chip for MEMS material property measurement using electrostatically actuated test structures, *J. MEMS* 6 (1997) 107–118.
- [20] <http://www.hysitron.com>, August 19, 2002.
- [21] <http://www.di.com>, August 19, 2002.
- [22] W.C. Oliver, G.M. Pharr, An improved technique for determining hardness and elastic modulus using load and displacement sensing indentation experiments, *J. Mater. Res.* 7 (1992) 1564–1583.
- [23] S. Adachi, *Physical Properties of III–V Semiconductor Compounds*, Wiley, New York, 1992.
- [24] D. Arivouli, R. Fornari, J. Kumar, Microhardness studies of doped and undoped InP crystals, *J. Mater. Sci. Lett.* 10 (1991) 559–561.
- [25] G. Keiser, *Optical Fiber Communications*, McGraw-Hill, Boston, MA, 2000.
- [26] W.D. Nix, Elastic and plastic properties of thin films on substrates: nanoindentation techniques, *Mater. Sci. Eng. A* 234–236 (1997) 37–44.
- [27] Y.G. Gogotsi, V. Domnich, S.N. Dub, A. Kailer, K.G. Nickel, Cyclic nanoindentation and Raman microspectroscopy of phase transformation in semiconductors, *J. Mater. Res.* 15 (2000) 871–879.
- [28] B. Bhushan, V.N. Koinkar, Microtribological studies of doped single-crystal silicon and polysilicon films for MEMS devices, *Sens. Actuators A* 57 (1996) 92–102.
- [29] J.N. Ding, Y.G. Meng, S.Z. Wen, Specimen size effect on mechanical properties of polysilicon microcantilever beams measured by deflection using a nanoindenter, *Mater. Sci. Eng. B* 83 (2001) 42–47.
- [30] B. Bhushan, X. Li, Micromechanical and tribological characterization of doped single-crystal and polysilicon films for micromechanical systems and devices, *J. Mater. Res.* 12 (1997) 54–63.